Published in "Physica Status Solidi (a) doi: 10.1002/pssa.201330680, 2014"
which should be cited to refer to this work.

Study of superconducting properties of ferrocene-added MgB_2

Sudesh[1], S. Das[2], C. Bernhard[2], T. Shripathi[3], and G. D. Varma*[,1]

[1] Department of Physics, Indian Institute of Technology Roorkee, Roorkee 247667, India
[2] Department of Physics, Fribourg Centre for Nanomaterials-FriMat, University of Fribourg, Chemin du Musee 3, 1700 Fribourg, Switzerland
[3] UGC-DAE CSR, University Campus, Khandwa Road, Indore 452001, India

Keywords critical current density, flux pinning, MgB_2 superconductor, upper critical field

* Corresponding author: e-mail gdvarfph@iitr.ac.in, Phone: +91 1332 285353, Fax: +91 1332 273560

In the present study, we have shown the effects of ferrocene ($FeC_{10}H_{10}$) addition on the superconducting properties of polycrystalline MgB_2 superconductor using transport and magnetic measurements. The addition of $FeC_{10}H_{10}$ up to 2 wt% in the MgB_2 sample has shown enhanced critical current density, J_C in the entire magnetic field region without affecting much the transition temperature. At 10 K, with respect to a pristine MgB_2 sample, J_C has improved by a factor of 6.55 at 6 T applied field for 1 wt% $FeC_{10}H_{10}$. An improvement in the upper critical field, H_{C_2} and irreversibility field, H_{irr} has also been observed up to 2 wt% addition of $FeC_{10}H_{10}$. The value of $H_{C_2}(0)$ as obtained using the Ginzburg–Landau (GL) – theory fit of the experimental data increases by almost 2 T for 2 wt% $FeC_{10}H_{10}$-added MgB_2 as compared to the pristine samples. From X-ray photoemission spectroscopy (XPS), we observed that the Fe is present in sample in the form of ferromagnetic oxides, Fe_3O_4 and γ-Fe_2O_3. These ferromagnetic inclusions provide efficient pinning centers to improve $J_C(H)$ behavior. The flux pinning mechanisms present in the $FeC_{10}H_{10}$-added samples are described and discussed in this paper.

1 Introduction The discovery of the MgB_2 superconductor in 2001 by the group of Akimitsu [1] has generated a lot of interest in this material. As compared to the high temperature cuprate superconductors and the low temperature superconductors, MgB_2 has a number of interesting and promising properties, which provide an opportunity to use this material in various technological applications. MgB_2 presents a significantly high superconducting critical temperature, $T_C = 39$ K than the low temperature superconductors. Although its T_C is much lower than the cuprates, the absence of weak link effects at the grain boundaries [2, 3] allows for a rather large dissipationless flow of critical current density, J_C, which is technologically very important. Furthermore, the two band-gap superconductivity in MgB_2 gives an opportunity to increase the upper critical field, H_{C_2}, another important thermodynamic quantity for technological application, through doping of elements at the Mg and B-sites. Samples have been grown with compositions $Mg_{1-x}Y_xB_2$ (Y = Al, Be, Li, and transition metal) [4–10] and $Mg(B_{1-x}Z_x)_2$, (Z = C) [11] to study the effect of doping at Mg and B sites, respectively, on the structural, electronic, and the superconducting properties of MgB_2. So far, the doping with carbon-containing compounds is found to be much more successful and effective in improving H_{C_2} and J_C. The carbon substitution for B enhances the intra-band scattering rate in the σ-band without affecting much the inter-band scattering leading to an enhancement of H_{C_2} [12, 13]. In addition, C doping improves the pinning strength by creating lattice distortion [14]. Among the various carbon sources, SiC nanoparticles [15, 16], carbon-nanotubes (CNT) [17], B_4C [18], graphene [19, 20], and carbohydrates [21, 22] have been very effective in improving H_{C_2} and $J_C(H)$. However, carbon doping introduces an extra electron in the conduction band of MgB_2, which reduces the hole density-of-states and leads to a reduction of the critical temperature, T_C [23]. In addition to carbon, addition of rare-earth oxides [24, 25] and dispersed magnetic nanoparticles [26] into MgB_2 have shown improvements in $J_C(H)$ and the irreversibility field, H_{irr}. Magnetic element substitution has always been considered to suppress superconductivity because it hinders Cooper pair formation, but it has been found that the effect of magnetic element substitution is the same as that of a non-magnetic element in case of a multi-band gap superconductor [27]. In MgB_2, however, the magnetic element doping is

observed to deteriorate the superconducting properties. The addition of various transition metal elements such as Cu, Co, Mn, and Fe has been used to study the effect of magnetism on the superconducting properties of MgB_2 [6, 9, 28–30]. Among the magnetic elements, Fe is found to behave as non-magnetic after substitution in MgB_2 system as only a meager change in T_C occurs with Fe substitution[30]. The effect of Fe doping in MgB_2 is of particular interest as it is widely used as the sheath material in fabricating wires. Fe has been used in the form of Fe-nanoparticles [26], Fe_3O_4-nanoparticles [31], and carbon-containing compounds of Fe [32] to study the pinning effect of Fe on superconductivity in MgB_2. Among these dopants, Fe_3O_4 has shown improvements in J_C, H_{C_2}, and H_{irr} of MgB_2 at high temperatures. Recently, doping of Fe in the form of carbon-encapsulated Fe nanoparticles has improved H_{C_2} and J_C in the entire field region [33].

In the present work, we have used ferrocene ($FeC_{10}H_{10}$) as a source of both carbon and iron to study the combined effect of adding Fe and C into the MgB_2 matrix on its superconducting properties. $FeC_{10}H_{10}$ is composed of Fe-metal attached to two aromatic hydrocarbon rings of C_5H_5. At temperatures higher than 500 °C, $FeC_{10}H_{10}$ decomposes completely to $Fe + H_2 + CH_4 + C_5H_6 + \ldots$ as well as reactive hydrocarbons [34]. The polycrystalline samples have been prepared with compositions $MgB_2 + x$ wt% $FeC_{10}H_{10}$ ($x = 0$, 1, 2, 3, and 5). X-ray diffraction results show a small decrease in the lattice parameters a and c, possibly due to a small C substitution at the B-site. An interesting result of $FeC_{10}H_{10}$ addition is that T_C remains almost unchanged up to 5 wt% addition of $FeC_{10}H_{10}$. However, as compared to pristine MgB_2, we have observed a significant improvement in J_C in the entire magnetic field range (0–7 T) at 10 and 20 K in the $FeC_{10}H_{10}$-added samples. The maximum improvement in $J_C(H)$ is observed for 1 wt% addition of $FeC_{10}H_{10}$. For this sample at 10 K, the value of J_C improves by a factor of 6.55 at 6 T applied field. Furthermore, an enhancement by about 2 T is observed for $H_{C_2}(0)$ as obtained with a GL-theory fit for the 2 wt% $FeC_{10}H_{10}$-added MgB_2 sample.

2 Experimental A series of $FeC_{10}H_{10}$-added samples with compositions $MgB_2 + x$ wt% $FeC_{10}H_{10}$ ($x = 0$, 1, 2, 3, and 5) was prepared using a solid-state reaction route. Appropriate amounts of Mg (Sigma–Aldrich, 99.9% pure) and B (Sigma–Aldrich, amorphous, 99%) were mixed with x wt% ($x = 0$, 1, 2, 3, and 5) of $FeC_{10}H_{10}$ (HiMedia, 98%) in an agate mortar. In order to account for the Mg loss, we have added 5 wt% extra Mg to all the compositions. The mixing was done thoroughly for about an hour and the powder was pressed into rectangular pellets. The pellets were placed in a soft iron tube and then sintered at 850 °C in a reducing atmosphere of Ar/H_2 (9/1) for 3 h followed by furnace cooling to room temperature. The crystalline structure of the samples was studied using X-ray diffractometry with Cu Kα radiation (1.5406 Å) over an angular (2θ) range between 10° and 80°. The microstructure of the samples was studied using a field emission scanning electron microscope (FE-SEM) (FEI-QUANTA 200 FEG). The core level X-ray photoemission spectra (XPS) were recorded using VSW make spectrometer (Al Kα radiation) at UGC-DAE-CSR, Indore, India. The spectral resolution was ~1 eV. The sample surfaces were cleaned before recording the spectra. The resistivity measurement in different magnetic fields (0–8 T) was carried out using a Physical Property Measurement System (PPMS) (Quantum Design-6000) at the University of Fribourg. The irreversibility fields (H_{irr}) and upper critical field ($H_{C_2}(T)$) were deduced using the criteria 10 and 90% of normal state resistivity for different applied fields, respectively. The DC magnetic measurements were carried out using Superconducting Quantum Interference Device (SQUID) magnetometer (Quantum Design MPMS XL). Transition temperature T_C was defined as the onset of the transition, and the magnetic J_C was estimated from the width of the magnetization loop ΔM at different field in the M–H loop, measured at temperatures 10 and 20 K, using the Bean's critical state model [35], $J_C = 20\Delta M/[Va(1 - a/3b)]$, where $\Delta M = M(+\text{ive}) - M(-\text{ive})$ in the positive applied field region of M–H loop, V is the volume, a and b are the length and width of the rectangular samples used for magnetization measurements.

3 Results and discussion Figure 1 shows the room temperature X-ray diffraction patterns of the pure and $FeC_{10}H_{10}$-added polycrystalline samples of MgB_2. The X-ray diffraction patterns for all the samples were refined using X'pert Highscore software. All samples are composed of a P6/mmm, hexagonal majority phase with only small amounts of MgO and unreacted Mg impurity phases. The volume percentage of MgO content in the samples is calculated using the formula: $X = (\sum \text{peak intensities of impurity phase} / \sum \text{peak intensities of all phases}) \times 100$. The values of the

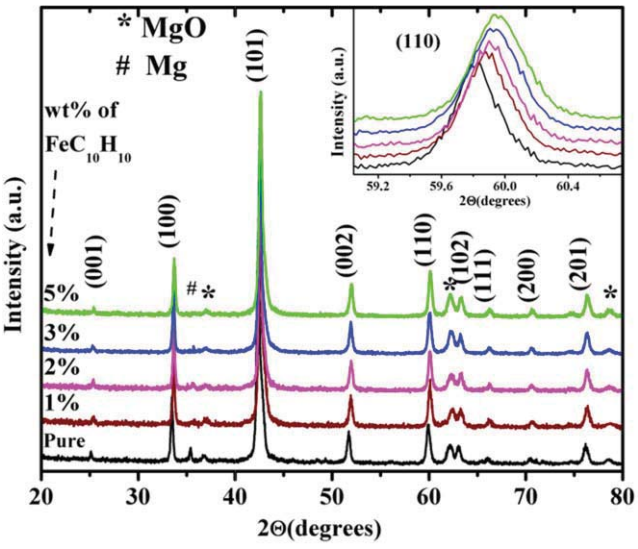

Figure 1 X-ray diffraction patterns of pure and $FeC_{10}H_{10}$-added MgB_2 samples. Inset shows the expanded part of the pattern for the (110) peak.

Table 1 Lattice parameters, FWHM, strain, MgO content, T_C (onset), $\Delta\rho$, RRR, and $H_{C_2}(0)$ of pristine and ferrocene-added samples.

x	a (Å)	c (Å)	FWHM (110)	strain (%)	MgO (%)	T_C (K)	$\Delta\rho$	RRR	$H_{C_2}(0)$
0	3.0889 (6)	3.5338 (9)	0.1495	0.036	14.76	38.76	71.32	3.084	17.414
1	3.0854 (5)	3.5288 (7)	0.1557	0.165	14.38	38.60	67.91	2.874	19.474
2	3.0849 (4)	3.5276 (5)	0.1596	0.170	13.85	38.54	60.51	2.662	19.543
3	3.0848 (7)	3.5270 (9)	0.1866	0.274	15.59	38.33	62.34	2.114	18.671
5	3.0845 (3)	3.5255 (5)	0.1855	0.226	13.45	38.08	58.47	2.459	18.158

MgO content, lattice parameters: a and c, the full width at half maximum (FWHM) of the (110) peak and the strain in the samples are listed in Table 1. The observed lattice parameters a and c for pure MgB_2 sample are: $a = 3.0889$ Å and $c = 3.5338$ Å, which are consistent with the literature values [36]. We observe that with increasing the level of $FeC_{10}H_{10}$ addition, the lattice parameters a and c decrease slightly. This slight decrease is possibly due to substitution of carbon for boron. The former is released from the decomposition of $FeC_{10}H_{10}$ above 500 °C. The lattice parameter changes observed in this study are similar to the aromatic hydrocarbon doped MgB_2 [37, 38].

Figure 2a–c shows the FESEM micrographs of pure, 1 and 3 wt% $FeC_{10}H_{10}$-added MgB_2 samples, respectively. It can be clearly seen that the average grain size of the samples decreases with increasing the level of $FeC_{10}H_{10}$ addition into the samples. This result is in conformity with the FWHM values listed in Table 1 for (110) plane. Figure 2d shows the EDX spectrum of the sample $MgB_2 + 3$ wt% $FeC_{10}H_{10}$. It clearly shows the presence of Fe in the samples. From the EDX studies, it is observed that the quantity of Fe increases with increasing addition of $FeC_{10}H_{10}$. However, we did not see any peak of Fe or its compounds in the XRD curves. This could be due to small quantity of Fe in the system, i.e., below the detection limit of XRD.

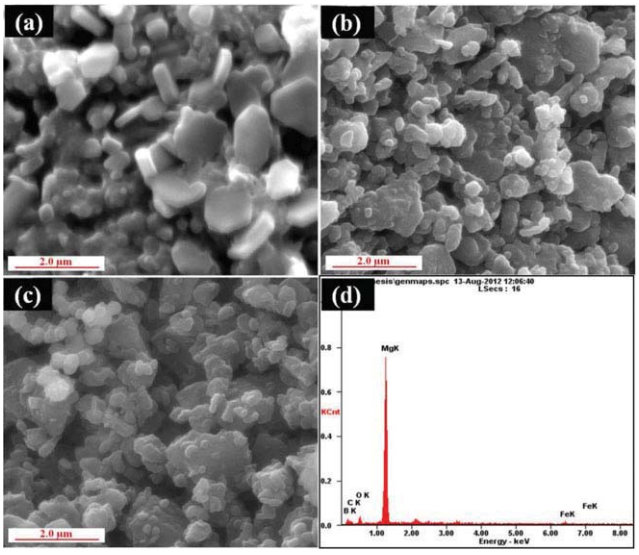

Figure 2 FESEM micrographs of (a) pure, (b) 1 wt% $FeC_{10}H_{10}$, and (c) 3wt% $FeC_{10}H_{10}$-added MgB_2 samples. (d) EDX pattern for the 3 wt% $FeC_{10}H_{10}$-added sample.

To know the state in which Fe is present in the MgB_2 matrix, XPS measurements for Fe 2p core level for 5 wt% $FeC_{10}H_{10}$ sample was performed. The deconvolution of peaks present in the XPS spectrum (as shown in Fig. 3a) was done to explore oxidation states of Fe present in the sample. The peaks at ~711.0 and ~724.8 eV correspond to the Fe $2p_{3/2}$ and Fe $2p_{1/2}$ spin states of Fe^{3+} oxidation state, while the peaks at ~709.2 and ~722.8 eV correspond to the Fe $2p_{3/2}$ and Fe $2p_{1/3}$ spin states of Fe^{2+} oxidation state [39]. Satellite peaks of Fe^{3+} and Fe^{2+} are also observed at binding energies ~733.4 eV (Fe^{3+}), ~714.6 eV (Fe^{2+}), ~729.5 eV (Fe^{2+}), and ~718.9 eV (Fe^{3+}). The Fe 2p high-resolution spectrum of Fe in MgB_2 matrix confirms the presence of Fe_3O_4 phase [40]. The satellite peak at ~718.9 eV is a characteristic peak of Fe^{3+} in γ-Fe_2O_3. This study indicates the presence of Fe_3O_4 and γ-Fe_2O_3 [41] in the $FeC_{10}H_{10}$-added samples. These phases of iron oxide are expected to form when the sample is sintered at high-temperature even in inert atmosphere due to the presence of oxygen (present as contamination in the present case). The presence of these oxides in the $FeC_{10}H_{10}$-added samples is also confirmed from the magnetization measurements performed at room temperature. Figure 3b shows the field dependent magnetization (M–H loop) of all the samples. This figure clearly shows the ferromagnetic nature of $FeC_{10}H_{10}$-added samples at room temperature possibly due the presence of Fe_3O_4/γ-Fe_2O_3 in the MgB_2 matrix.

The temperature dependence of the resistivity of all the samples (measured from 5 to 300 K) normalized to the room temperature resistivity ($\rho(T)/\rho(300\,K)$) is shown in Fig. 4. The inset of Fig. 4 shows the superconducting transition for all the samples. It can be readily observed that there is a sharp superconducting transition in all the samples and a very small change in T_C is observed with addition of $FeC_{10}H_{10}$. The critical temperature, T_C, has been defined as the onset of the superconducting transition in the resistivity curves. The small decrease in T_C with addition of $FeC_{10}H_{10}$ suggests that there is no substitution of Fe in the MgB_2 lattice. The observed small decrease of T_C may be caused by disorder-induced scattering of the electrons due to a minor substitution of carbon for boron. The residual resistivity ratio, RRR ($=\rho(300\,K)/\rho(40\,K)$) is shown for all samples in Table 1. The value of RRR is maximum for the pure MgB_2 sample and it decreases with increasing $FeC_{10}H_{10}$ addition in samples. This also suggests an increase of the impurity or

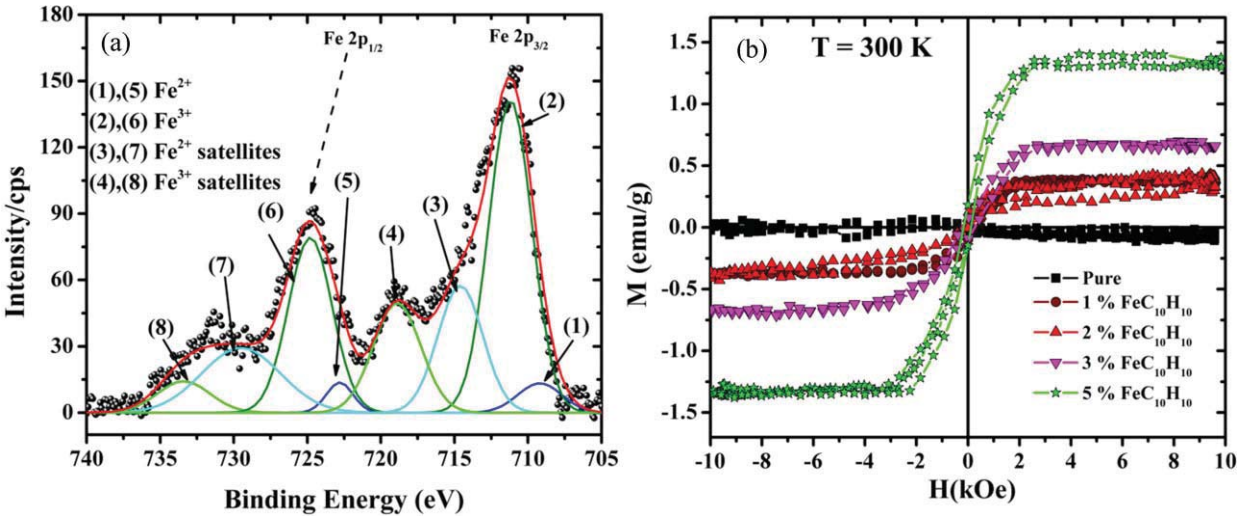

Figure 3 (a) Fe2p spectrum of 5 wt% ferrocene-added MgB_2 sample. The peaks are deconvoluted into eight peaks corresponding to different oxidation states and satellite peaks of Fe. (b) Magnetization (per gram of sample) versus applied magnetic field plot at room temperature for all the samples.

disorder-induced scattering rate with $FeC_{10}H_{10}$ addition. The variation of T_C with increasing addition of $FeC_{10}H_{10}$ is shown in Table 1.

The connectivity of the grains can be explored using the parameter $\Delta\rho$ ($=\rho(300\,K)-\rho(40\,K)$), as described by Rowell [42]. We observe that the value of $\Delta\rho$ decreases with increasing $FeC_{10}H_{10}$ addition into the samples, which tells us that the grain connectivity and thus the area fraction is enhanced with the addition of $FeC_{10}H_{10}$. This is also clear from the FESEM images of the $FeC_{10}H_{10}$-added samples. The larger value of $\Delta\rho$ and smaller value of RRR in the 3 wt% $FeC_{10}H_{10}$-added sample as compared to other samples is due to a larger amount of MgO in this sample as observed from XRD (see Table 1). The larger MgO content creates Mg deficiency, which gives rise to defects and hence larger strain in the sample as compared to other samples [43].

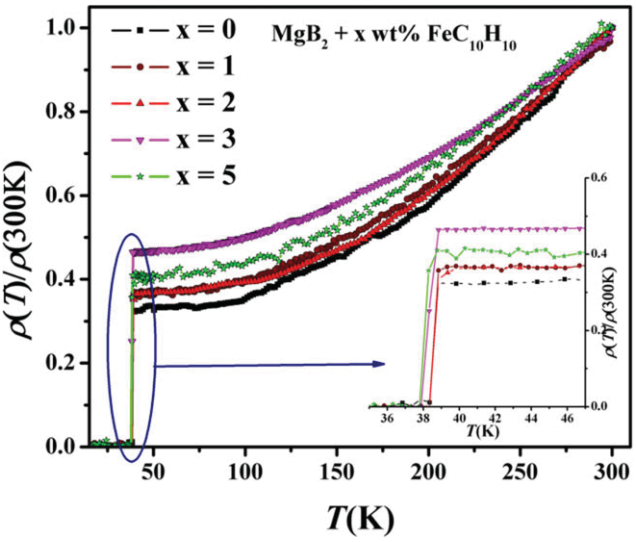

Figure 4 Resistivity versus temperature plots for the pure and the $FeC_{10}H_{10}$-added MgB_2 samples. Inset: enlarged view of the superconducting transition.

To determine the temperature dependence of H_{C_2} and H_{irr}, resistivity versus temperature measurements near the superconducting transition have been performed in an applied magnetic field of 0–8 T. Figure 5 shows the resistivity curves for all the samples in different applied fields in the range 0–8 T. From these resistivity curves, the values of H_{C_2} and H_{irr} have been deduced using the criteria of 90 and 10% of normal state resistivity. The plots of H_{C_2} and H_{irr} versus reduced temperature, T/T_C are shown in Fig. 6a and b, respectively. From Fig. 6a, we observe an improvement in H_{C_2} with addition of $FeC_{10}H_{10}$ in MgB_2. The values of the upper critical field, $H_{C_2}(0)$ is calculated by fitting the $H_{C_2}(T)$ versus T/T_C plot with the Ginzburg–Landau (GL) theory [44]: $H_{C_2}(T) = H_{C_2}(0)[(1-t^2)/(1+t^2)]$, where $t = T/T_C$ is the reduced temperature. The maximum value of $H_{C_2}(0) = 19.54$ T is found for the sample with 2 wt% added $FeC_{10}H_{10}$. This value of $H_{C_2}(0)$ is comparable to the one reported in Ref. [45] for nano-magnetic particle doped MgB_2. From Fig. 6b, we see an improvement in $H_{irr}(T)$ due to the addition of $FeC_{10}H_{10}$. This is suggestive of an enhanced pinning in the $FeC_{10}H_{10}$-added samples as compared to pristine one. In Fig. 7a and b, we have shown the magnetic hysteresis (M–H) loops for all the samples at 10 and 20 K, respectively. Inset in Fig. 7a and b shows the enlarged view of hysteresis loops in high field region at 10 and 20 K, respectively. This figure shows that M–H loops at 10 K remain open up to a field of 7 T except for pure MgB_2 sample. This again confirms the improvement in H_{irr} of $FeC_{10}H_{10}$-added MgB_2 samples. The critical current density at different fields of all the $FeC_{10}H_{10}$-added samples is calculated using the M–H loops measured at 10 and 20 K.

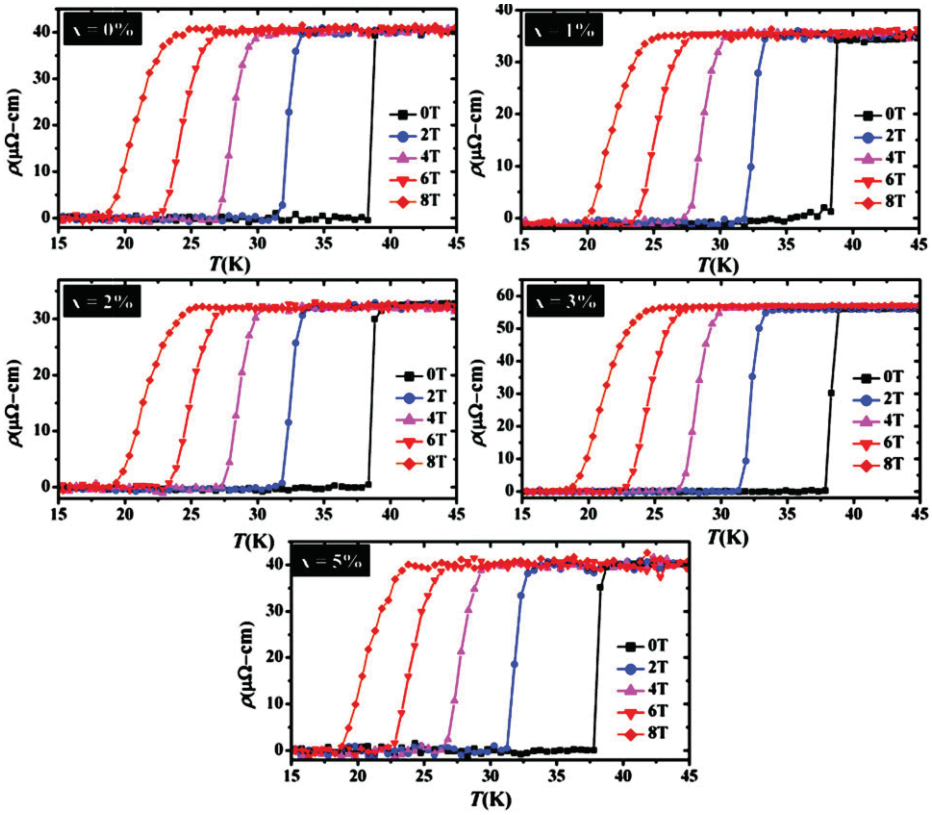

Figure 5 The magnetoresistance plots at different applied magnetic fields (0–8 T) for all the samples.

For this, we used the modified Bean's model [35]: $J_C = 20\,\Delta M/[Va(1 - a/3b)]$, where $\Delta M = M(+\text{ive}) - M(-\text{ive})$ in the positive applied field region of M–H loop, V is the volume, a and b are the length and width of the rectangular samples used for magnetization measurements. The values of J_C at 10 K and 20 K in applied magnetic fields of 1.5 T and 5 T are shown in Table 2. Figure 8a and b depicts the critical current density, J_C versus applied magnetic field (H) (1–7 T) behavior of all the samples at 10 and 20 K, respectively. This figure shows a substantial improvement in J_C of 1 and 2 wt% $FeC_{10}H_{10}$-added MgB_2 samples with respect to pristine MgB_2 in the magnetic field range 1–7 T at both 10 and 20 K. For the 3 wt% $FeC_{10}H_{10}$-added sample, there is only a marginal improvement in J_C over the pristine MgB_2. For the 5 wt% $FeC_{10}H_{10}$-added sample J_C at 10 K becomes lower than that of the pure sample in the magnetic field range 0–6 T. However, at fields greater than 6 T it still shows an improvement over the pristine sample. At 20 K, J_C of 5 wt%

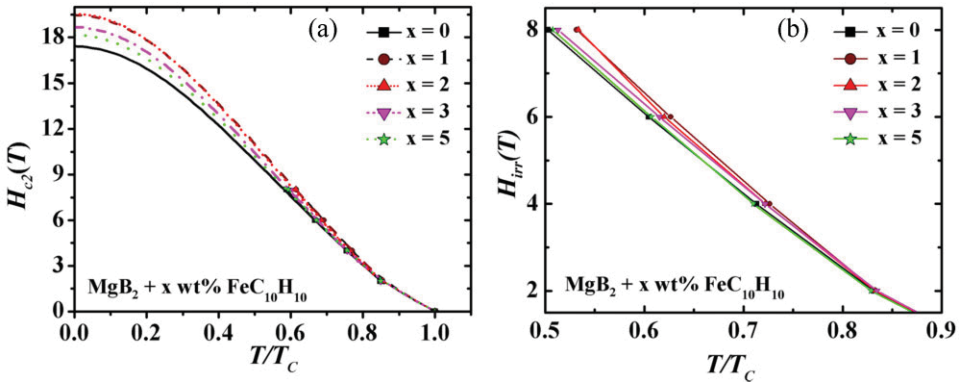

Figure 6 (a) Upper critical field, H_{C_2} and (b) irreversibility field, H_{irr} as a function of the reduced temperature, T/T_C, determined using a 90 and 10% criterion of the normal state resistivity, respectively. In (a), we have shown the GL-fit of the experimental data extended to 0 K for $x = 0$ (straight line, black), 1 (dashed, wine), 2 (short-dotted, red), 3 (dash-dotted, magenta), and 5 (dotted, green).

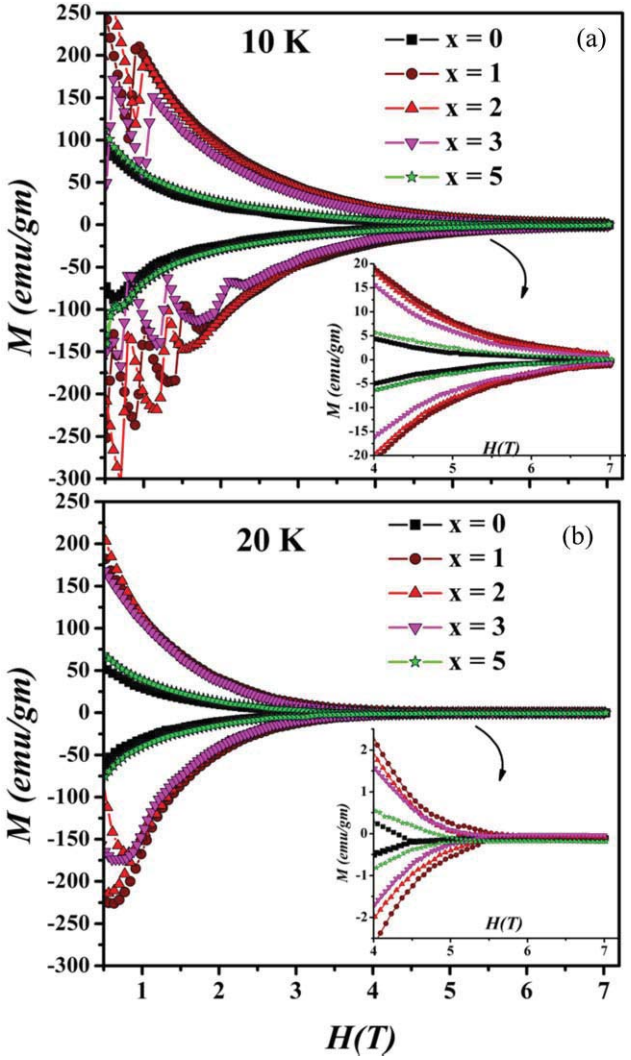

Figure 7 Magnetic hysteresis loops (0.5–7 T) for all the samples at (a) 10 K and (b) 20 K. Insets: enlarged view of *M–H* loops in the high field region 4–7 T for all the samples at (a) 10 K and (b) 20 K.

$FeC_{10}H_{10}$-added sample is comparable to pristine sample in the magnetic field range 0–4 T and for fields greater than 4 T, J_C of this sample has higher values as compared to pure sample (see Fig. 8b). There is an improvement in J_C in the magnetic field range 0–1 T at both temperatures up to a level of 2 wt% $FeC_{10}H_{10}$ addition; however, at 10 K due to flux jump effect some fluctuations in $J_C(H)$ have been observed in this field range. In earlier studies, a similar type of flux jumps in MgB_2 samples has been reported [46, 47]. This phenomenon is mainly governed by the flux-jump instability of the critical state in a type-II superconductor and is determined by the strong pinning and thermomagnetic properties of these materials [48]. Flux jumps are mainly observed in the nanoparticle-doped samples [49, 50], which prove to be effective pinning centers thus giving rise to high critical currents. For 2 wt% $FeC_{10}H_{10}$-added sample at 20 K, we have observed a fish-tail effect in $J_C(H)$ plot in the field range 5–6 T (see inset in Fig. 8b). This type of effect has been reported earlier in carbon doped MgB_2 polycrystalline sample and it is suggested that it occurs due to the disorder created by carbon substitution [51].

Table 2 Critical current density, J_C values at 10 and 20 K for all the samples.

x (%)	J_C (A cm^{-2})			
	10 K		20 K	
	1.5 T ($\times 10^5$)	5 T ($\times 10^3$)	1.5 T ($\times 10^4$)	5 T ($\times 10^3$)
0	1.63	0.78	0.82	0.11
1	7.83	4.37	4.13	2.15
2	9.72	4.37	4.73	1.09
3	2.42	1.43	1.31	0.37
5	1.79	0.99	1.11	0.30

To understand the flux pinning mechanism present in the samples, we have calculated the volume-pinning force density, F_p ($F_p = J_C(H) \times H$) from the $J_C(H)$ behavior. In Fig. 9a and b, we have shown f_p ($=F_p/F_p^{max}$) versus normalized applied magnetic field, h ($=H/H_{max}$) for all the samples at 10 and 20 K, respectively. The normalized volume pinning force, f_p, in high temperature superconductors often scales with H/H_{irr} [52]. However, it is difficult to calculate the accurate value of H_{irr} from the dc magnetization measurements. In order to avoid this problem, the data are often scaled with H/H_{max} ($=h$) instead of H/H_{irr} [52–54], as done in the present case. The scaling for $f(h)$ is often analyzed with the help of the following equations for different flux pinning mechanisms:

$$f_p = 3h^2\left(1 - \frac{2h}{3}\right), \delta k - \text{pinning}, \quad (1)$$

$$f_p = \frac{9}{4}h\left(1 - \frac{h}{3}\right)^2, \delta T_C - \text{pinning}, \quad (2)$$

$$f_p = \frac{25}{16}\sqrt{h}\left(1 - \frac{h}{5}\right)^2, \text{surface} - \text{pinning}. \quad (3)$$

From the $f_p(h)$ curves (Fig. 9a and b), we observe that in the pure MgB_2 sample, the dominant pinning mechanism at 10 and 20 K is mainly the surface/grain boundary pinning. With increasing addition of $FeC_{10}H_{10}$ concentration (and hence the precipitates of ferromagnetic Fe_3O_4/γ-Fe_2O_3), we observe that the $f_p(h)$ curve shifts more toward the theoretical curve for δT_C or point pinning. So, in the present case the presence of ferromagnetic iron-oxide inclusions act as effective point pinning centers, which lead to improvement in $J_C(H)$ behavior in the entire magnetic field region. This result is similar to the improved $J_C(H)$ behavior of $FeC_{10}H_{10}$-grafted polysiloxane doped MgB_2 samples due to the point pinning on Fe-oxides [55].

Thus, by adding $FeC_{10}H_{10}$ into the MgB_2 samples, we have observed improvement in $J_C(H)$ in the entire magnetic

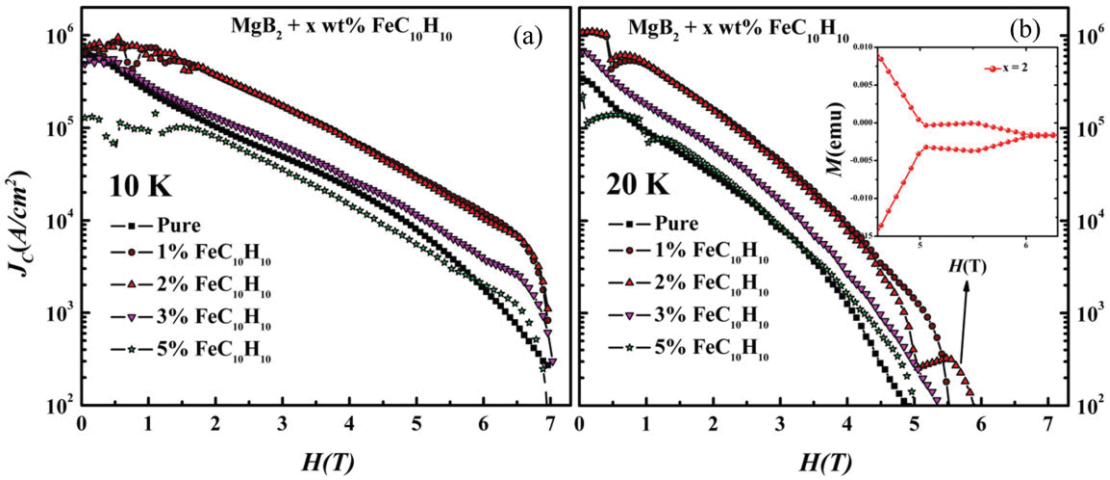

Figure 8 Critical current density versus magnetic field (J_C (H)) plots at 10 K (a) and 20 K (b) for all the $MgB_2 + x$ wt% $FeC_{10}H_{10}$ ($x = 0$, 1, 2, 3, and 5) samples, inset shows the enlarged view of M–H plot at high field values for 2 wt% $FeC_{10}H_{10}$-added sample showing fish-tail effect.

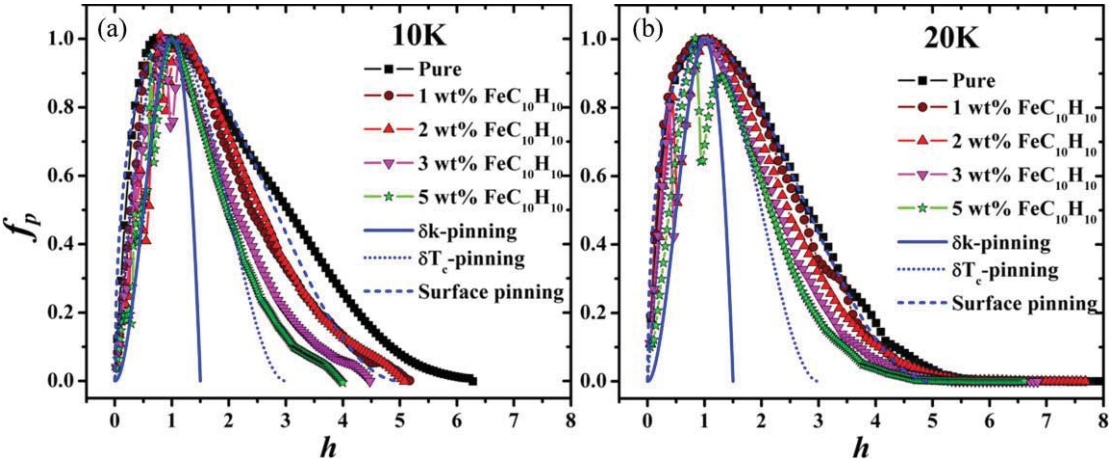

Figure 9 Magnetic field h ($=H/H_{max}$) dependence of flux pinning force density, f_p ($=F_p/F_p^{max}$) of all the samples at (a) 10 K and (b) 20 K. The solid line represents δk-pinning, short-dotted line represents δT_C-pinning and short-dashed line represents surface pinning corresponding to Eqs. (1)–(3), respectively (see text).

field region. After decomposition at temperatures above ~500 °C, $FeC_{10}H_{10}$ provides two types of additives, iron and carbon. It is clear from the variation of the lattice parameters and the superconducting transition temperature with increasing the weight percentage concentration of $FeC_{10}H_{10}$ that there is a very small substitution of Fe and C into the MgB_2 lattice. The XPS study done on 5 wt% $FeC_{10}H_{10}$-added samples suggests that the Fe is present in the samples in oxidized form of a mixture of Fe_3O_4 and γ-Fe_2O_3, which are also confirmed from the magnetization measurements done at room temperature. The small substitution of carbon atoms for B in this study is similar to the aromatic hydrocarbon doping done in previous studies [37, 38]. Fe in the form of ferromagnetic oxides (Fe_3O_4/γ-Fe_2O_3) and carbon substitution lead to the improved $J_C(H)$ behavior in the entire magnetic field region. The results obtained for improved $J_C(H)$ performance in the present case are comparable to n-SiC doped MgB_2 samples at high fields, while the self field J_C is better than n-SiC doped MgB_2 samples [15, 16].

4 Conclusions In the present work, we have studied the effect of $FeC_{10}H_{10}$ addition on the superconducting properties of the MgB_2 compound. The superconducting critical current density, J_C is significantly improved with increasing $FeC_{10}H_{10}$ concentration into the sample in the entire magnetic field region (0–7 T) while the transition temperature is hardly affected up to an addition level of 2 wt%. The upper critical field for the optimal added concentration of $FeC_{10}H_{10}$ in the sample has improved by ~2 T. The maximum $H_{C_2}(0)$ as calculated from the GL-fit is found to be 19.54 T for the 2 wt% $FeC_{10}H_{10}$-added MgB_2.

Acknowledgments One of the authors, Sudesh is thankful to the Ministry of Human Resources and Development (MHRD), India for providing the financial support. S. Das and C. Bernhard acknowledge funding by the Swiss National Science Foundation (SNF) Grant No. 200020-140225 and by Project No. 122935 of the Indo-Swiss Joint Research Program (ISJRP).

References

[1] J. Nagamatsu, N. Nakagawa, T. Muranaka, Y. Zenitani, and J. Akimitsu, Nature **410**, 63–64 (2001).
[2] Y. Bugoslavsky, G. K. Perkins, X. Qi, L. F. Cohen, and A. D. Caplin, Nature **410**, 563–565 (2001).
[3] D. C. Larbalestier, L. D. Cooley, M. O. Rikel, A. A. Polyanskii, J. Jiang, S. Patnaik, X. Y. Cai, D. M. Feldmann, A. Gurevich, A. A. Squitieri, M. T. Naus, C. B. Eom, E. E. Hellstrom, R. J. Cava, K. A. Regan, N. Rogado, M. A. Hayward, T. He, J. S. Slusky, P. Khalifah, K. Inumaru, and M. Haas, Nature **410**, 186–189 (2001).
[4] S. Agrestini, C. Metallo, M. Filippi, L. Simonelli, G. Campi, C. Sanipoli, E. Liarokapis, S. De Negri, M. Giovannini, A. Saccone, A. Latini, and A. Bianconi, Phys. Rev. B **70**, 134514 (2004).
[5] J. S. Ahn, Y. J. Kim, M. S. Kim, S. I. Lee, and E. J. Choi, Phys. Rev. B **65**, 172503 (2002).
[6] M. Kuhberger and G. Gritzner, Physica C **370**, 39–43 (2002).
[7] I. Pallecchi, P. Brotto, C. Ferdeghini, M. Putti, A. Palenzona, P. Manfrinetti, A. G. Lehmann, A. Orecchini, C. Petrillo, F. Sacchetti, M. Affronte, G. Allodi, R. De Renzi, S. Serventi, A. Andreone, G. Lamura, D. Daghero, R. S. Gonnelli, and M. Tortello, Supercond. Sci. Technol. **22**, 095014 (2009).
[8] J. S. Slusky, N. Rogado, K. A. Regan, M. A. Hayward, P. Khalifah, T. He, K. Inumaru, S. M. Loureiro, M. K. Haas, H. W. Zandbergen, and R. J. Cava, Nature **410**, 343–345 (2001).
[9] A. Tampieri, G. Celotti, S. Sprio, D. Rinaldi, G. Barucca, and R. Caciuffo, Solid State Commun. **121**, 497–500 (2002).
[10] J. Y. Xiang, D. N. Zheng, J. Q. Li, L. Li, P. L. Lang, H. Chen, C. Dong, G. C. Che, Z. A. Ren, H. H. Qi, H. Y. Tian, Y. M. Ni, and Z. X. Zhao, Phys. Rev. B **65**, 214536 (2002).
[11] M. Paranthaman, J. R. Thompson, and D. K. Christen, Physica C **355**, 1–5 (2001).
[12] M. Angst, S. L. Bud'ko, R. H. T. Wilke, and P. C. Canfield, Phys. Rev. B **71**, 144512 (2005).
[13] A. V. Sologubenko, N. D. Zhigadlo, S. M. Kazakov, J. Karpinski, and H. R. Ott, Phys. Rev. B **71**, 020501 (2005).
[14] S. K. Chen, X. Xu, J. H. Kim, S. X. Dou, and J. L. MacManus-Driscoll, Supercond. Sci. Technol. **22**, 125005 (2009).
[15] S. X. Dou, A. V. Pan, S. Zhou, M. Ionescu, X. L. Wang, J. Horvat, H. K. Liu, and P. R. Munroe, J. Appl. Phys. **94**, 1850–1856 (2003).
[16] A. Vajpayee, V. P. S. Awana, G. L. Bhalla, and H. Kishan, Nanotechnology **19**, 125708 (2008).
[17] S. X. Dou, W. K. Yeoh, J. Horvat, and M. Ionescu, Appl. Phys. Lett. **83**, 4996–4998 (2003).
[18] A. Yamamoto, J. Shimoyama, S. Ueda, I. Iwayama, S. Horii, and K. Kishio, Supercond. Sci. Technol. **18**, 1323 (2005).
[19] K. S. B. De Silva, S. Gambhir, X. L. Wang, X. Xu, W. X. Li, D. L. Officer, D. Wexler, G. G. Wallace, and S. X. Dou, J. Mater. Chem. **22**, 13941–13946 (2012).
[20] K. S. B. De Silva, X. Xu, X. L. Wang, D. Wexler, D. Attard, F. Xiang, and S. X. Dou, Scr. Mater. **67**, 802–805 (2012).
[21] N. Ojha, V. K. Malik, R. Singla, C. Bernhard, and G. D. Varma, Supercond. Sci. Technol. **22**, 125014 (2009).
[22] X. P. Zhang, D. L. Wang, Z. S. Gao, L. Wang, Y. P. Qi, Z. Y. Zhang, Y. W. Ma, S. Awaji, G. Nishijima, K. Watanabe, E. Mossang, and X. Chaud, Supercond. Sci. Technol. **23**, 025024 (2010).
[23] J. Kortus, O. V. Dolgov, R. K. Kremer, and A. A. Golubov, Phys. Rev. Lett. **94**, 027002 (2005).
[24] N. Ojha, V. K. Malik, C. Bernhard, and G. D. Varma, Phys. Status Solidi A **207**, 175–182 (2010).
[25] N. Ojha, V. K. Malik, C. Bernhard, and G. D. Varma, Physica C **469**, 846–851 (2009).
[26] T. Kuroda, T. Nakane, H. Uematsu, and K. Kumakura, Supercond. Sci. Technol. **19**, 1152 (2006).
[27] A. A. Golubov and I. I. Mazin, Phys. Rev. B **55**, 15146–15152 (1997).
[28] P. J. T. Joseph and P. P. Singh, Solid State Commun. **141**, 390–393 (2007).
[29] K. Rogacki, B. Batlogg, J. Karpinski, N. D. Zhigadlo, G. Schuck, S. M. Kazakov, P. Wagli, R. Puzniak, A. Wisniewski, F. Carbone, A. Brinkman, and D. van der Marel, Phys. Rev. B **73**, 174520 (2006).
[30] Y. D. Gao, J. Ding, G. V. S. Rao, and B. V. R. Chowdari, J. Appl. Phys. **93**, 8656–8658 (2003).
[31] B. Qu, X. D. Sun, J. G. Li, Z. M. Xiu, S. H. Liu, and C. P. Xue, Supercond. Sci. Technol. **22**, 015027 (2009).
[32] S. H. Zhou and S. X. Dou, Solid State Sci. **12**, 105 (2010).
[33] V. Sandu, G. Aldica, S. Popa, P. Badica, E. Cimpoiasu, F. Dumitrache, and E. Sandu, J. Appl. Phys. **110**, 123921 (2011).
[34] A. Barreiro, S. Hampel, M. H. Rummeli, C. Kramberger, A. Gruneis, K. Biedermann, A. Leonhardt, T. Gemming, B. Buchner, A. Bachtold, and T. Pichler, J. Phys. Chem. B **110**, 20973–20977 (2006).
[35] C. P. Bean, Rev. Mod. Phys. **36**, 9 (1985).
[36] C. H. Cheng, Y. Zhao, X. T. Zhu, J. Nowotny, C. C. Sorrell, T. Finlayson, and H. Zhang, Physica C **386**, 588–592 (2003).
[37] H. Yamada, M. Hirakawa, H. Kumakura, and H. Kitaguchi, Supercond. Sci. Technol **19**, 175–177 (2006).
[38] H. Yamada, N. Uchiyama, H. Kumakura, H. Kitaguchi, and A. Matsumoto, IEEE Trans. Appl. Supercond. **17**, 2850–2853 (2007).
[39] T. Yamashita and P. Hayes, Appl. Surf. Sci. **254**, 2441–2449 (2008).
[40] T. Fujii, F. M. F. de Groot, G. A. Sawatzky, F. C. Voogt, T. Hibma, and K. Okada, Phys. Rev. B **59**, 3195–3202 (1999).
[41] H. Liu, E. Y. Jiang, R. K. Zheng, and H. L. Bai, Phys. Status Solidi A **201**, 739–744 (2004).
[42] J. M. Rowell, Supercond. Sci. Technol. **16**, R17 (2003).
[43] A. Serquis, X. Z. Liao, Y. T. Zhu, J. Y. Coulter, J. Y. Huang, J. O. Willis, D. E. Peterson, F. M. Mueller, N. O. Moreno, J. D. Thompson, V. F. Nesterenko, and S. S. Indrakanti, J. Appl. Phys. **92**, 351–356 (2002).
[44] X. Wang, S. R. Ghorbani, G. Peleckis, and S. Dou, Adv. Mater. **21**, 236–239 (2009).
[45] W. Li and S. X. Dou, in: Superconductor, edited by A. M. Luiz (Sciyo, Croatia, 2010), pp. 111–134.
[46] I. Felner, V. P. S. Awana, M. Mudgel, and H. Kishan, J. Appl. Phys. **101**, 09G101 (2007).
[47] V. P. S. Awana, M. Isobe, K. P. Singh, E. Takayama-Muromachi, and H. Kishan, Supercond. Sci. Technol. **19**, 551 (2006).

[48] Y. Kimishima, S. Takami, T. Okuda, M. Uehara, T. Kuramoto, and Y. Sugiyama, Physica C **463**, 281–285 (2007).
[49] S. X. Dou, V. Braccini, S. Soltanian, R. Klie, Y. Zhu, S. Li, X. L. Wang, and D. Larbalestier, J. Appl. Phys. **96**, 7549–7555 (2004).
[50] G. J. Xu, J. C. Grivel, A. B. Abrahamsen, and N. H. Andersen, Physica C **406**, 95–99 (2004).
[51] Q. Cai, Y. Liu, Z. Ma, and D. A. Cardwell, Physica C **492**, 6–10 (2013).
[52] T. Higuchi, S. I. Yoo, and M. Murakami, Phys. Rev. B **59**, 1514–1527 (1999).
[53] Z. X. Shi, Y. X. Zhang, H. Lv, M. Xu, E.-M. Choi, and S.-I. Lee, Physica C **467**, 101–105 (2007).
[54] I. Shigeta, T. Abiru, K. Abe, A. Nishida, and Y. Matsumoto, Physica C **392–396**, 359–363 (2003).
[55] V. Sandu, E. Cimpoiasu, G. Aldica, S. Popa, E. Sandu, B. St. Vasile, N. Hurduc, and I. Nor, Physica C **480**, 102–107 (2012).